

# Phase-field model and its splitting numerical scheme for tissue growth



Darae Jeong, Junseok Kim\*

Department of Mathematics, Korea University, Seoul 136-713, Republic of Korea

## ARTICLE INFO

### Article history:

Received 18 May 2015  
 Received in revised form 29 July 2016  
 Accepted 30 January 2017  
 Available online 3 February 2017

### Keywords:

Cahn–Hilliard equation  
 Tissue growth  
 Operator splitting method  
 Multigrid method

## ABSTRACT

We consider phase-field models and associated numerical methods for tissue growth. The model consists of the Cahn–Hilliard equation with a source term. In order to solve the equations accurately and efficiently, we propose a hybrid method based on an operator splitting method. First, we solve the contribution from the source term analytically and redistribute the increased mass around the tissue boundary position. Subsequently, we solve the Cahn–Hilliard equation using the nonlinearly gradient stable numerical scheme to make the interface transition profile smooth. We then perform various numerical experiments and find that there is a good agreement when these computational results are compared with analytic solutions.

© 2017 IMACS. Published by Elsevier B.V. All rights reserved.

## 1. Introduction

The mathematical modeling and computational simulation of tumor growth dynamics can yield important insights into tumor progression, help to explain experimental and clinical observations, and help with assessing optimal treatment strategies [28]. Much research has focused on modeling tumor growth using a diffuse interface model, in which sharp interfaces are replaced by narrow transition layers (see [7,28], and references therein). The building block in the diffuse interface model is the Cahn–Hilliard (CH) equation [5]. The CH equation exhibits useful properties, such as separating two different materials in modeling interface problems. However, it has some drawbacks in the case of modeling tissue growth. When we model tissue growth with the CH equation we add an extra source term to the equation. If the proliferation rate is large, then the volume fraction becomes greater than one, which is far from the physical quantity. We note that the tumor growth model has been studied in order to explain the complex dynamics of the behavior of tumor cells. General reviews relating to tumor growth can be found in [1,21,24]. For mass balances in cellular biological media, see [13,14], and for a summary relating to the shape of tumors, see [23]. Applications of diffuse-interface tumor growth models have recently been proposed in relation to both tumor growth [11,12] and surfaces of tumor mass [10]. The evolution of tumors has also been described using a reaction–diffusion equation in [2].

The main purpose of this paper is to present a phase-field model for application to fundamental tissue growth along with accurate and efficient numerical solutions. In comparison with conventional tumor growth models using phase-field methods [6,22,26,28,29], the proposed model admits useful features, such as keeping the minimum and maximum of the volume fraction close to zero and one, an ability to handle large values for the proliferation parameter, and yielding a

\* Corresponding author. Fax: +82 2 929 8562.

E-mail address: [cfdkim@korea.ac.kr](mailto:cfdkim@korea.ac.kr) (J. Kim).

URL: <http://math.korea.ac.kr/~cfdkim/> (J. Kim).

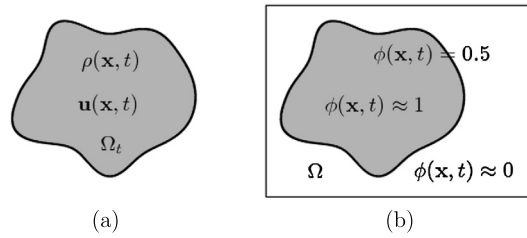


**Fig. 1.** Schematic of the tumor in the phase-field model. In (a)  $\rho(\mathbf{x}, t)$  represents the density,  $\mathbf{u}(\mathbf{x}, t)$  the velocity field, and  $\Omega_t$  the domain of the tumor. (b) displays that  $\phi(\mathbf{x}, t)$  is approximately 1 on the inside and 0 on the outside of the tumor. The interface of the tumor is represented as  $\phi(\mathbf{x}, t) = 0.5$ .

robust and accurate numerical scheme. In particular, the first feature is important from a physical point of view, because the volume fraction should not be greater than one.

The rest of the paper is organized as follows. In Section 2, we describe a mathematical model for tissue growth. In Section 3, we provide a new numerical method for the tissue growth model. We perform several numerical experiments on the effect of the proposed method in Section 4. In Section 5, we provide a summary and present our conclusions.

### 2. Mathematical model

We develop a simple mathematical model for describing the dynamics of early stage of tumor growth in the absence of a necrotic core. Let  $\rho(\mathbf{x}, t)$  be the density of the tumor and  $\mathbf{u}(\mathbf{x}, t)$  the velocity field in the tumor at position  $\mathbf{x}$  and time  $t$ . The conservation of mass gives

$$\rho_t(\mathbf{x}, t) + \nabla \cdot [\rho(\mathbf{x}, t)\mathbf{u}(\mathbf{x}, t)] = \lambda_p \rho(\mathbf{x}, t) \text{ in } \Omega_t, \tag{1}$$

where  $\lambda_p$  is the proliferation rate and  $\Omega_t$  is the tumor domain [3] (see Fig. 1).

Let us assume that the density in the tumor is constant, i.e.,  $\rho(\mathbf{x}, t) \equiv \rho_0$ . Then, Eq. (1) becomes

$$\nabla \cdot \mathbf{u}(\mathbf{x}, t) = \lambda_p \text{ in } \Omega_t. \tag{2}$$

In order to develop a phase-field model for Eq. (1), let us introduce the phase-field function  $\phi$ , which is the volume fraction of the tumor cell. Therefore,  $\phi \approx 1$  in the tumorous phase  $\Omega_t$  and  $\phi \approx 0$  in the healthy tissue phase  $\Omega \setminus \Omega_t$ . The function also has a smooth transition between 0 and 1. We interpret the level set,  $\phi = 0.5$ , as the tissue interface. First, we extend the tissue domain to  $\Omega$  which is time-independent and embeds  $\Omega_t$ . Then, we can approximate with  $\rho = \rho_0\phi$  in  $\Omega$ . Plugging this into Eq. (1), we have

$$\phi_t(\mathbf{x}, t) + \nabla \cdot [\phi(\mathbf{x}, t)\mathbf{u}(\mathbf{x}, t)] = \lambda_p \phi(\mathbf{x}, t) \text{ in } \Omega.$$

Under the assumption that the density is constant, the effect of the velocity field  $\mathbf{u}$  is to distribute the increased mass to the boundary of the tissue. We model this advection term with a relaxation term in the CH equation, i.e.,  $-M\Delta[F'(\phi(\mathbf{x}, t)) - \epsilon^2\Delta\phi(\mathbf{x}, t)]$ , where  $M$  represents mobility,  $F(\phi) = 0.25\phi^2(\phi - 1)^2$ , and  $\epsilon$  is a small positive parameter. Therefore, the proposed model for Eq. (1) is given as

$$\phi_t(\mathbf{x}, t) = M\Delta\mu(\mathbf{x}, t) + \lambda_p\phi(\mathbf{x}, t), \mathbf{x} \in \Omega, t > 0, \tag{3}$$

$$\mu(\mathbf{x}, t) = F'(\phi(\mathbf{x}, t)) - \epsilon^2\Delta\phi(\mathbf{x}, t), \tag{4}$$

where  $\mu$  is the chemical potential and  $\epsilon$  is the gradient energy coefficient related to the following total energy of the system (3)-(4) with  $\lambda_p = 0$ .

$$\mathcal{E} = \int_{\Omega} (F(\phi) + 0.5\epsilon^2|\nabla\phi|^2) \, d\mathbf{x} \tag{5}$$

The boundary conditions are  $\frac{\partial\phi}{\partial\mathbf{n}} = \frac{\partial\mu}{\partial\mathbf{n}} = 0$  on  $\partial\Omega$ , where  $\mathbf{n}$  is the outward normal vector to the domain boundary  $\partial\Omega$ .

We note that if  $\lambda_p = 0$ , then Eqs. (3) and (4) reduce to the classical CH equation. The CH equation, a fourth-order parabolic equation was originally derived to describe the phase separation and coarsening phenomena in a melted binary alloy [4,5]. For further details on the physical, mathematical, and numerical derivations of the binary CH equation, see the review paper [19,25].

### 3. Numerical method

In this section, we propose an efficient and accurate numerical method, based on an operator splitting technique for solving the governing Eqs. (3) and (4).

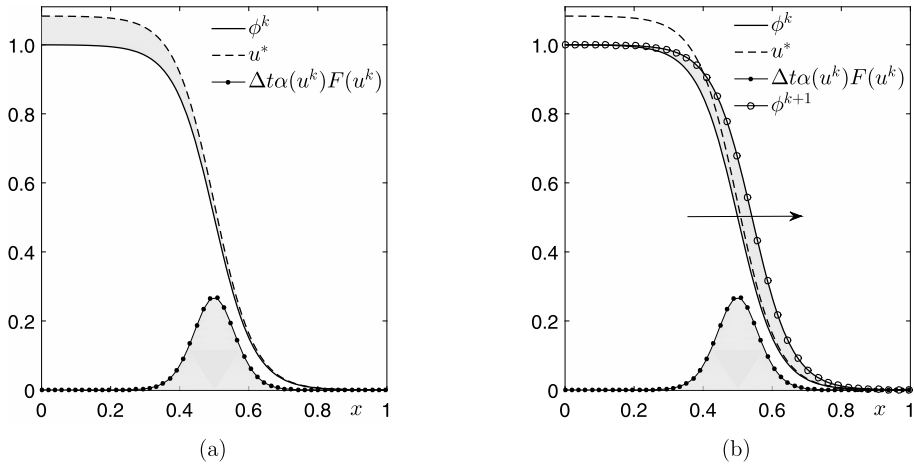


**Fig. 2.** Schematic illustration of the proposed numerical method. (a) Increased mass (gray-colored region) representing in Eq. (11). (b) Redistributed mass by CH Eqs. (12)–(13).

### 3.1. One-dimensional space

First, we consider the governing equations in a one-dimensional space with  $\Omega = (a, b)$ . For the sake of simplicity, we set  $M = 1$  unless otherwise specified in Eq. (3). We define  $\phi$  at  $(x_i, t_k)$ , where  $x_i = a + (i - 0.5)h$  for  $i = 1, \dots, N_x$  and  $t_k = k\Delta t$  for  $k = 1, \dots, N_t$ . Here,  $N_x$  and  $N_t$  are the total numbers of grid points in  $x$  and  $t$ , respectively. Furthermore,  $h = (b - a)/N_x$  is the spatial step size and  $\Delta t = T/N_t$  is the temporal step size, where  $T$  is the final time. For convenience, we use the notation  $\phi_i^k = \phi(x_i, t_k)$ . One possible discretization of Eqs. (3) and (4) is the nonlinearly gradient stabilized scheme type [8,9] as follows:

$$\begin{aligned} \frac{\phi_i^{k+1} - \phi_i^k}{\Delta t} &= \frac{1}{h^2} (\mu_{i+1}^{k+1} - 2\mu_i^{k+1} + \mu_{i-1}^{k+1}) + \lambda_p \phi_i^k, \\ \mu_i^{k+1} &= (\phi_i^{k+1})^3 - 1.5(\phi_i^{k+1})^2 + 0.75\phi_i^{k+1} - 0.25\phi_i^k \\ &\quad - \frac{\epsilon^2}{h^2} (\phi_{i+1}^{k+1} - 2\phi_i^{k+1} + \phi_{i-1}^{k+1}). \end{aligned}$$

This discretization is called the bulk growth model. We propose another model. By applying the operator splitting method, we split Eqs. (3) and (4) formally as

$$u_t(x, t) = \lambda_p u(x, t) \quad \text{with } t \in [t^k, t^{k+1}], \quad u(x, t^k) = \phi^k \tag{6}$$

$$v_t(x, t) = \mu_{xx}(x, t) \quad \text{with } t \in [t^k, t^{k+1}], \quad v(x, t^k) = u(x, t^{k+1}), \tag{7}$$

$$\mu(x, t) = F'(v(x, t)) - \epsilon^2 v_{xx}(x, t), \tag{8}$$

where the approximated solution by splitting algorithm at the point  $t = t^{k+1}$  is defined as  $\phi^{k+1} = v(x, t^{k+1})$ .

Our first step is to solve Eq. (6) analytically. That is,

$$u_i^* = u_i^k e^{\lambda_p \Delta t} \quad \text{for } i = 1, \dots, N_x. \tag{9}$$

Subsequently, we redistribute the increased mass around the interfacial region by matching the total mass as shown in Fig. 2(a). Therefore, the numerical solution is defined as follows.

$$u_i^{k+1} = u_i^k + \Delta t \alpha(u^k) F(u_i^k), \quad \text{for } i = 1, \dots, N_x \tag{10}$$

where  $u_i^{k+1}$  satisfies  $\sum_{i=1}^{N_x} u_i^{k+1} = \sum_{i=1}^{N_x} u_i^*$ . Then,  $\alpha(t)$  is given as

$$\alpha(u^k) = \frac{e^{\lambda_p \Delta t} - 1}{\Delta t} \sum_{i=1}^{N_x} u_i^k / \sum_{i=1}^{N_x} F(u_i^k). \tag{11}$$

Fig. 2 shows the schematic of this process.

Finally, we obtain  $v^{k+1}$  by solving the CH equations (7) and (8), using the nonlinearly gradient stable scheme [8,9]:

$$\frac{v_i^{k+1} - v_i^k}{\Delta t} = \frac{1}{h^2} (\mu_{i+1}^{k+1} - 2\mu_i^{k+1} + \mu_{i-1}^{k+1}), \tag{12}$$

$$\begin{aligned} \mu_i^{k+1} &= (v_i^{k+1})^3 - 1.5(v_i^{k+1})^2 + 0.75v_i^{k+1} - 0.25v_i^k \\ &\quad - \frac{\epsilon^2}{h^2} (v_{i+1}^{k+1} - 2v_i^{k+1} + v_{i-1}^{k+1}), \end{aligned} \tag{13}$$

for  $i = 1, \dots, N_x$ . Therefore, the increased mass in Eq. (10) is distributed along the interface of  $v$  by Eq. (12)–(13) (see Fig. 2(b)). We employ a multigrid method [27] for solving the resulting discrete system of equations (12) and (13). The multigrid method is widely used for solving the CH equation in two-dimensional [15,18,20], three-dimensional [17], and axisymmetric [16] domains. In this study, we refer to the algorithm (9)–(13) as the surface-limited growth model. Note that the proposed algorithm does not evolve according to Eq. (6). However, we only use Eq. (6) for the purpose of measuring the increased volume and then redistribute the additional volume to the surface area. In later sections, we will highlight the difference between the two models.

### 3.2. Radially and spherically symmetric coordinates

Next, we consider numerical solutions in radially and spherically symmetric coordinates. The governing equations are expressed as

$$u_t(r, t) = \lambda_p u(r, t), \quad \text{with } t \in [t^n, t^{n+1}], \quad u(x, t^n) = \phi^n, \tag{14}$$

$$v_t(r, t) = \frac{1}{r^d} (r^d \mu_r(r, t))_r, \quad \text{with } t \in [t^n, t^{n+1}], \quad v(x, t^n) = u(x, t^{n+1}), \tag{15}$$

$$\mu(r, t) = F'(v(r, t)) - \frac{\epsilon^2}{r^d} (r^d v_r(r, t))_r. \tag{16}$$

Here,  $u_t$  and  $u_r$  represent the partial derivatives of  $u$  with respect to  $t$  and  $r$ , respectively. The other notation is defined in the same manner. Also,  $d = 1$  and  $d = 2$  denote the radially and spherically symmetric coordinates, respectively. We discretize the domain  $\Omega = (0, a)$ . Let  $r$  be the variable in the radial or spherical direction. We define the cell center as  $r_i = (i - 0.5)h$  and the cell edge as  $r_{i+\frac{1}{2}} = hi$ , for  $i = 1, \dots, N_r$ . Here,  $N_r$  is the number of cells in the  $r$  direction and  $h = a/N_r$  is the spatial step size. We use the notation  $\phi_i^k = \phi(r_i, t^k)$ . First, we solve Eq. (14) using an analytic solution as

$$u_i^* = u_i^n e^{\lambda_p \Delta t}.$$

Similar to the one-dimensional case, to allocate the increased mass  $\sum_{i=1}^{N_r} 2d\pi r_i^d (u_i^* - u_i^k)h$  on the interfacial region, we use the following equation:

$$u_i^{k+1} = u_i^k + \Delta t \alpha(u^k) F(u_i^k),$$

where  $\alpha(u^k) = (e^{\lambda_p \Delta t} - 1) \sum_{i=1}^{N_r} r_i^d u_i^k / (\Delta t \sum_{i=1}^{N_r} r_i^d F(u_i^k))$ . Then, we solve the CH equations (15) and (16), as

$$\begin{aligned} \frac{v_i^{k+1} - v_i^k}{\Delta t} &= \frac{1}{h^2} \left[ \left( \frac{r_{i+\frac{1}{2}}}{r_i} \right)^d (\mu_{i+1}^{k+1} - \mu_i^{k+1}) - \left( \frac{r_{i-\frac{1}{2}}}{r_i} \right)^d (\mu_i^{k+1} - \mu_{i-1}^{k+1}) \right], \\ \mu_i^{k+1} &= (v_i^{k+1})^3 - 1.5(v_i^{k+1})^2 + 0.75v_i^{k+1} - 0.25v_i^k \\ &\quad - \frac{\epsilon^2}{h^2} \left[ \left( \frac{r_{i+\frac{1}{2}}}{r_i} \right)^d (v_{i+1}^{k+1} - v_i^{k+1}) - \left( \frac{r_{i-\frac{1}{2}}}{r_i} \right)^d (v_i^{k+1} - v_{i-1}^{k+1}) \right]. \end{aligned}$$

### 4. Numerical experiments

In this section, we present our numerical results. It follows from our choice of the equilibrium profile that  $\phi(x) = 0.5 - 0.5 \tanh(x/(2\sqrt{2}\epsilon))$  on an infinite domain, the concentration field varies from 0.05 to 0.95 over a distance of about  $4\sqrt{2}\epsilon \tanh^{-1}(0.9)$ . If we want this value to be approximately  $m$  grid points, then we choose the value of  $\epsilon$  to be

$$\epsilon_m = hm/[4\sqrt{2} \tanh^{-1}(0.9)], \tag{17}$$

where  $h$  is the grid size.

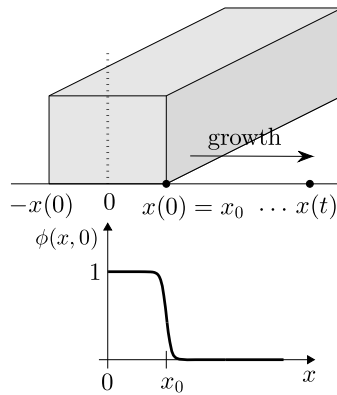


**Fig. 3.** Top: a symmetric one-dimensional tumor with the initial boundary positions  $x(0) = x_0$ . Bottom: a computational domain with symmetric boundary condition at  $x = 0$ .

**Table 1**

Errors and rates of convergence with respect to different spatial and temporal step sizes. (Theoretical position:  $x_{th} = 0.66402338$ .)

$\Delta t$	0.02	0.01	0.005	0.0025
$h$	1/32	1/64	1/128	1/256
$x_{num}$	0.660629	0.662863	0.663513	0.663813
$e_h$	0.003394	0.001160	0.000510	0.000211
ratio		1.549	1.186	1.276

#### 4.1. One-dimensional growth

Now, we consider a one-dimensional growth process.

In Fig. 3, the top and bottom figures show a symmetric one-dimensional tumor with the initial boundary positions  $x(0) = x_0$  and a computational domain with a symmetric boundary condition at  $x = 0$ , respectively.

From Eq. (2), we have that  $u(x(t), t) = \lambda_p x(t)$ . From the fact that the outermost cells in the tumor are moving at the same velocity of the expansion of the tumor, we have that

$$\frac{dx(t)}{dt} = u(x(t), t) = \lambda_p x(t).$$

Therefore, the position of the tumor  $x(t)$  by proliferation is represented as

$$x(t) = x(0)e^{\lambda_p t}, \tag{18}$$

where  $x(0)$  is the initial position of the tumor.

##### 4.1.1. Convergence test

We perform convergence test with various temporal and spatial step sizes. For this, we investigate the convergence of the position  $x$  satisfying  $\phi(x, t) = 0.5$  with the reference value  $x_{th} = x_0 e^{\lambda_p T}$  from Eq. (18). Here, we assume that the initial tumor is modeled by

$$\phi(x, 0) = \frac{1}{2} - \frac{1}{2} \tanh\left(\frac{x - x_0}{2\sqrt{2}\epsilon}\right), \tag{19}$$

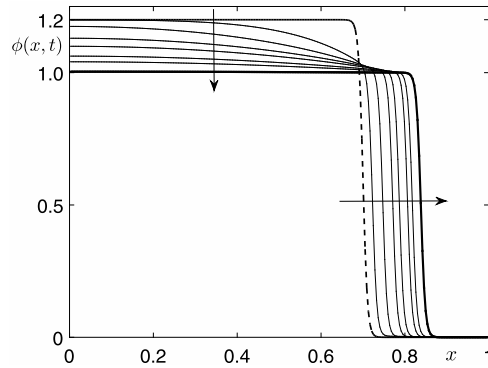
where  $x_0$  is the initial tissue boundary position. Also, the numerical parameters used are  $\lambda_p = 0.02$ ,  $\epsilon = 0.01501$ ,  $x_0 = 0.2$ ,  $T = 60$ , and  $\Omega = (0, 1)$ .

Table 1 shows the resulting errors and rates of convergence with respect to various spatial and temporal step sizes. With the theoretical value  $x_{th} = 0.66402338$ , we calculate the error which is defined as  $e_h := |x_{num} - x_{th}|$ . Here,  $x_{num}$  is the position of  $x$  that satisfies  $\phi(x, T) = 0.5$ . We define the rate of convergence as the ratio of successive errors, that is,  $\log_2(e_h/e_{h/2})$ . As shown in Table 1, we observe a first-order accuracy with respect to space and time. We also observe that the position  $x$  seems to converge towards the theoretical position for decreasing temporal and spatial step sizes. Therefore, in order to obtain accurate numerical results, we use  $\Delta t = 0.0025$ ,  $h = 1/256$  in the following simulations, unless otherwise specified.

Furthermore, we investigate the convergence of numerical solution with different  $\lambda_p$ . When we use  $\Delta t = 0.0025$ ,  $T = 20$ , and  $h = 1/256$  on  $\Omega = (0, 1)$ , we obtain the numerical results in Table 2. Through these results, we can see that numerical solution converges to the analytic solution regardless of  $\lambda_p$ .

**Table 2**  
Convergence of numerical solution with various  $\lambda_p$ .

$\lambda_p$	0.005	0.01	0.02	0.04	0.08
$x_{\text{num}}$	0.2210464	0.2443043	0.2984186	0.4452666	0.9919455
$x_{\text{th}}$	0.2210341	0.2442805	0.298364	0.4451081	0.9906064
$x_{\text{num}} - x_{\text{th}}$	0.0000122	0.0000237	0.0000536	0.0001584	0.0013390



**Fig. 4.** Dynamics of the Cahn–Hilliard equation with a stacked layer. Here, the dashed line, bold solid line, and arrows are the initial condition, final solution, and direction of time evolution, respectively.

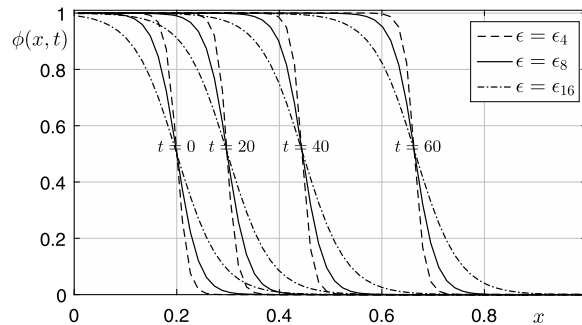


**Fig. 5.** Time evolution of  $\phi$  with different  $\epsilon$ . Here, the dashed, solid, and dash-dotted lines represent the numerical solutions using  $\epsilon_4$ ,  $\epsilon_8$ , and  $\epsilon_{16}$ , respectively.

4.1.2. Dynamics of the Cahn–Hilliard equation

In this section, we investigate the dynamics of the CH equation, for application to tumor tissue growth. For this, we solve the original CH equation given by (3) and (4) with  $\lambda_p = 0$ . We consider the following initial condition

$$\phi(x, 0) = 1.2 \left[ \frac{1}{2} - \frac{1}{2} \tanh \left( \frac{x - 0.7}{2\sqrt{2}\epsilon} \right) \right]$$

to express the situation for proliferation of the tissue. Here, the factor 1.2 is just used to make the proliferation as an example. In this test, we use the following parameters:  $\epsilon = \epsilon_8 \approx 0.00375$  and  $T = 2.5$ . As shown in Fig. 4, we can see the temporal evolution of the numerical results up to  $T = 2.5$ . In this figure, the dashed line, bold solid line, and arrows represent the initial condition, final solution, and direction of time evolution, respectively. As time increases,  $\phi$  which is larger than 1 decreases to 1 and the interface of  $\phi$  goes to the right side. This behavior can express cell growth by the proliferation.

4.1.3. Effect of  $\epsilon$

We now investigate the effect of  $\epsilon$ , which is related to the interface width. We perform a numerical simulation with the initial condition (19) with  $x_0 = 0.2$ . In this test, we take the proliferation rate  $\lambda_p = 0.02$  and  $T = 60$  on  $\Omega = (0, 1)$ . Here, we use  $h = 1/64$  as an exception to emphasize the effect of  $\epsilon$ .

Fig. 5 presents the numerical results with the three different values  $\epsilon_4$ ,  $\epsilon_8$ , and  $\epsilon_{16}$ . Here, the dashed, solid, and dash-dotted lines point to the numerical solutions by  $\epsilon_4$ ,  $\epsilon_8$ , and  $\epsilon_{16}$ , respectively.

As we expected, the smaller value of  $\epsilon$  leads to the more sharp transition layer. Also, we can see that the interface location is almost identical in Fig. 5.

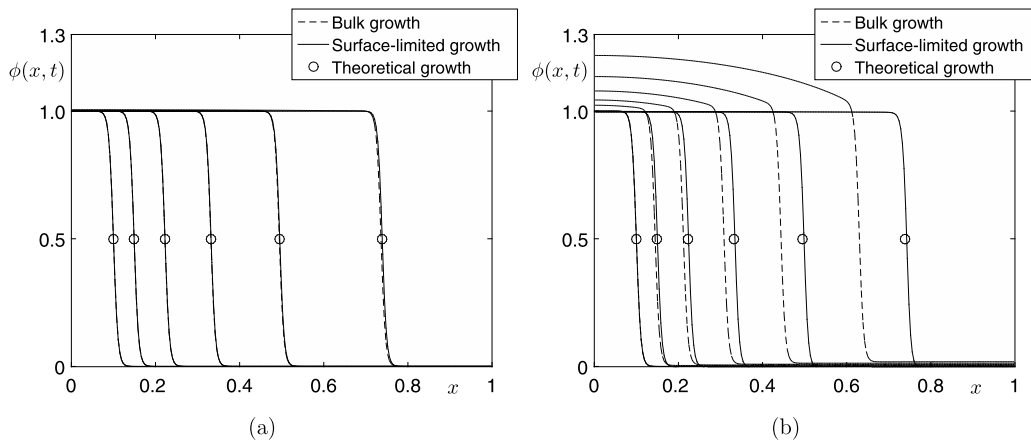


Fig. 6. Effect of  $\lambda_p$ . Time evolution of  $\phi$  with (a)  $\lambda_p = 0.01$  and (b)  $\lambda_p = 1$  in bulk growth, surface-limited growth, and a theoretical growth solution.

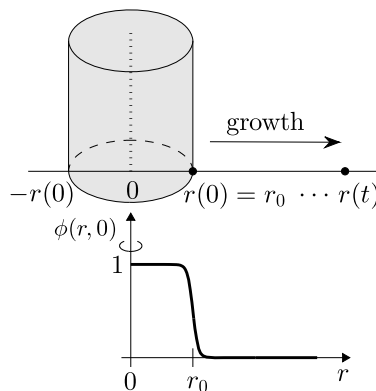


Fig. 7. Top: a radially symmetric two-dimensional tumor with the initial boundary position  $r(0) = r_0$ . Bottom: a computational domain with a symmetric boundary condition at  $r = 0$ .

4.1.4. Effect of  $\lambda_p$

We investigate the effect of  $\lambda_p$ . At the same time, we compare the difference between Model I of surface-limited growth and Model II of bulk growth. In this numerical test, we use the parameters  $\epsilon = \epsilon_8$ ,  $T = 9$ , and  $x_0 = 0.1$  with the initial condition (19). Also, we use two different values  $\lambda_p = 0.01$  and  $\lambda_p = 1$ . The time evolution of  $\phi$  for  $\lambda_p = 0.01$  and  $\lambda_p = 1$  are shown in Figs. 6(a) and (b), respectively.

When  $\lambda_p$  is small, the tumor shapes predicted by Model I and Model II are similar to the theoretical growth solution given by Eq. (18). From Fig. 6, we can see that the tumor of Model II (bulk growth) moves more slowly than that of Model I (surface-limited growth). However, when the proliferation rate  $\lambda_p$  is large, we can see that the tumor of Model II moves more slowly than that of Model I. The reason is that the Model I could not propagate the increased concentration on time. As the proliferation rate  $\lambda_p$  increases, the tumor concentration increases, instead of the propagation.

4.2. Two-dimensional growth

We now consider the surface-limited growth model on the radially-symmetric domain and the full two-dimensional domain.

Fig. 7 represents a schematic illustration of a radially symmetric domain.

In this radially symmetric domain, by Eq. (2), we have

$$\frac{1}{r} \frac{\partial}{\partial r} (ru(r(t), t)) = \lambda_p \quad \text{on } \Omega = [0, +\infty). \tag{20}$$

By integrating Eq. (20) and applying the zero homogeneous Neumann boundary condition at  $r = 0$ , i.e.,  $\frac{\partial u}{\partial r}(0, t) = 0$ , we obtain the theoretical position

$$r(t) = r_0 e^{\lambda_p t / 2}, \tag{21}$$

where  $r_0$  is the radius of the initial disk.

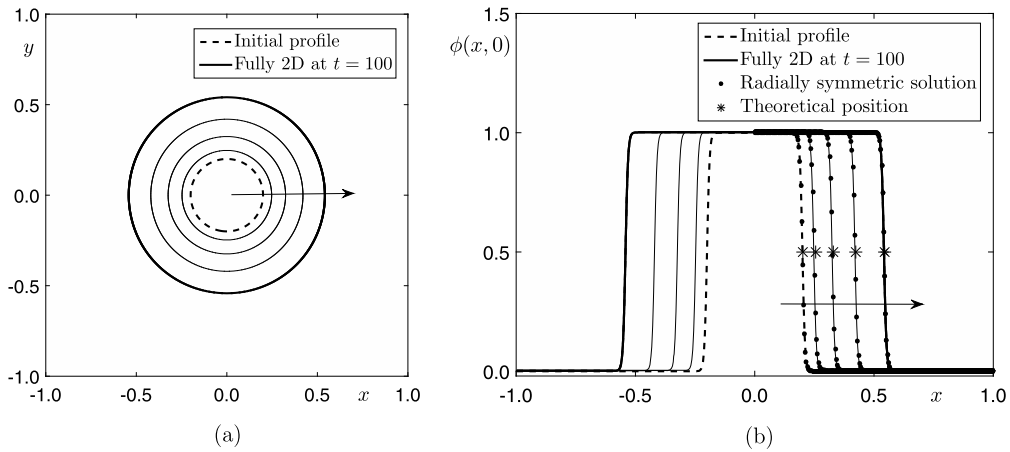


**Fig. 8.** Temporal evolutions of the radially symmetric and fully two-dimensional simulations with  $\lambda_p = 0.02$ . (a) Contour lines at the level  $\phi(x, y) = 0.5$  and (b) cross-section profiles at  $t = 0, 25, 50, 75,$  and  $100$ . Here, the arrow indicates the increasing time.

4.2.1. Temporal evolution

We now present the computational results for the radially symmetric and fully two-dimensional simulations. For the radially symmetric simulation, we set the following initial phase-field profile as

$$\phi(r, 0) = \frac{1}{2} - \frac{1}{2} \tanh\left(\frac{r - r_0}{2\sqrt{2}\epsilon}\right)$$

on the domain  $\Omega = (0, 1)$ . Also, for the fully two-dimensional simulation, we start with the following initial condition

$$\phi(x, y, 0) = \frac{1}{2} - \frac{1}{2} \tanh\left(\frac{\sqrt{x^2 + y^2} - r_0}{2\sqrt{2}\epsilon}\right)$$

on the domain  $\Omega = (-1, 1) \times (-1, 1)$ . Both numerical tests are used as  $r_0 = 0.2, \lambda_p = 0.02,$  and  $\epsilon = \epsilon_8$ . The other parameters are same to the previous one.

Fig. 8(a) represents the temporal evolutions of numerical solution by fully two-dimensional simulations up to  $t = 100$ . The result means the contour line of the numerical solution at the level  $\phi(x, y) = 0.5$  at  $t = 0, 25, 50, 75,$  and  $100$ . Here, the arrow indicates the increasing time. As shown in Fig. 8(a), the initial circle is getting bigger and this points out the tissue growth in two-dimensional domain. Also, Fig. 8(b) illustrates the cross-sectional view at  $y = 0$ . For verification of numerical results, we overlap the three different profiles by fully two-dimensional, radially symmetric, and theoretical solutions at specified times. A comparison of the numerical values and theoretical value shows that these are well matched each other.

4.2.2. Numerical stability test with  $\lambda_p$

In this section, we present numerical stability of the surface-limited growth model with the proliferation rate  $\lambda_p$ . For the initial condition, we consider the following elliptic shape tumor which is given by  $x^2/a^2 + y^2/b^2 = 1$ .

By Darcy’s law, we assume the cell velocity  $\mathbf{u} = -\nabla p$ , where  $p$  is the pressure field. Then, by using Eq. (2), we have that

$$-\Delta p = \nabla \cdot \mathbf{u} = \lambda_p. \tag{22}$$

As the pressure field is unique up to a constant, we set a zero Dirichlet boundary condition on the moving domain boundary  $\partial\Omega_t$ , where  $\partial\Omega_0 = \{(x, y) | x^2/a^2 + y^2/b^2 = 1\}$ . The solution for Eq. (22) is given as

$$p(x, y) = -\frac{\lambda_p a^2 b^2}{2(a^2 + b^2)} \left( \frac{x^2}{a^2} + \frac{y^2}{b^2} - 1 \right).$$

Then, we have the velocity

$$\mathbf{u}(x, y) = -\nabla p(x, y) = \frac{\lambda_p}{a^2 + b^2} (b^2 x, a^2 y). \tag{23}$$

Here, we can derive  $a$  and  $b$  analytically. We set the initial points of the major and minor axes of the ellipse as  $a_0$  and  $b_0$ . The time derivative equations are obtained from Eq. (23):

$$\frac{da}{dt} = \frac{\lambda_p b^2 a}{a^2 + b^2}, \quad \frac{db}{dt} = \frac{\lambda_p a^2 b}{a^2 + b^2}.$$



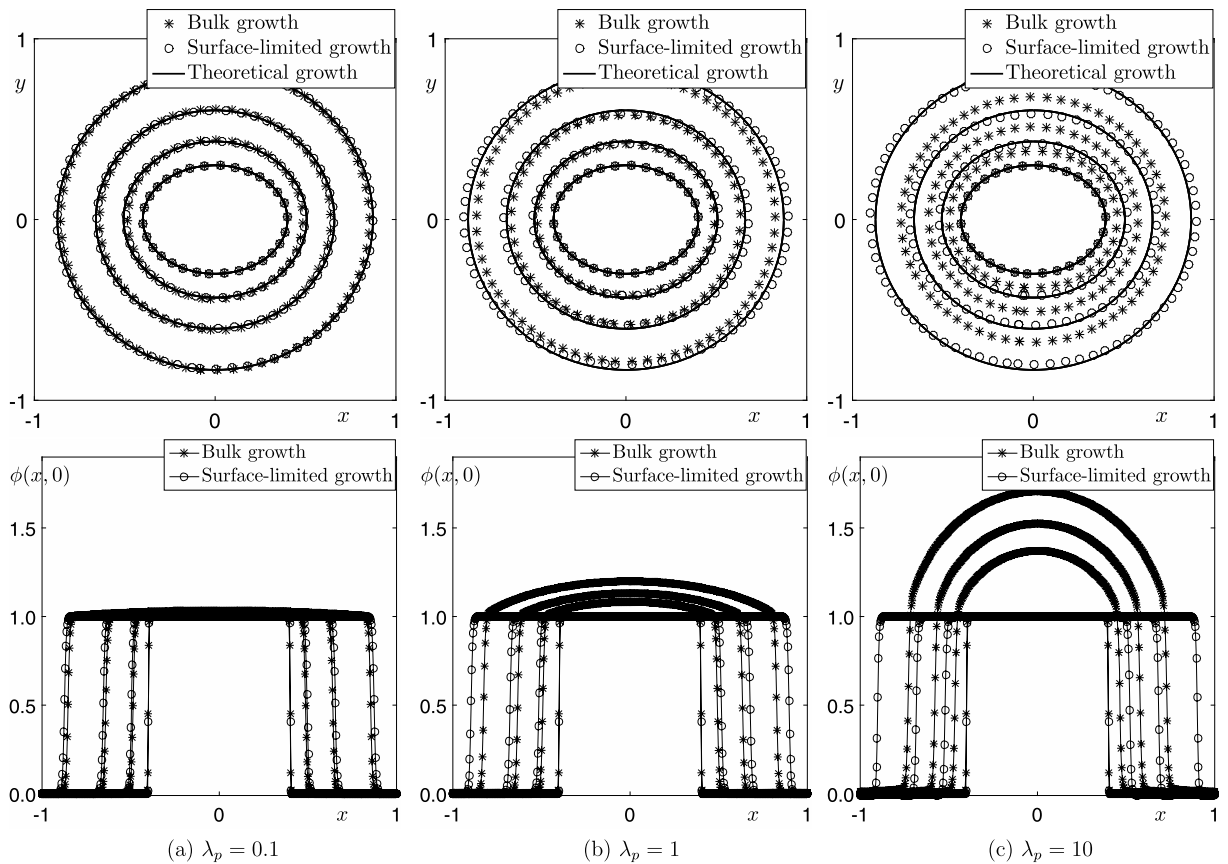


**Fig. 9.** Comparison of temporal solutions by the bulk, surface-limited, and theoretical growth with respect to (a)  $\lambda_p = 0.1$ , (b)  $\lambda_p = 1$ , and (c)  $\lambda_p = 10$ . Here, the first and second rows represent the contour line at 0.5 level and the cross section of  $\phi$ , respectively.

The solutions are then given by

$$a(t) = \sqrt{a_0^2 - b_0^2 + \sqrt{a_0^4 - 2a_0^2b_0^2 + b_0^4 + 4a_0^2b_0^2e^{2\lambda_p t}}/\sqrt{2}}, \tag{24}$$

$$b(t) = \sqrt{b_0^2 - a_0^2 + \sqrt{a_0^4 - 2a_0^2b_0^2 + b_0^4 + 4a_0^2b_0^2e^{2\lambda_p t}}/\sqrt{2}}, \tag{25}$$

where we suppose that  $a_0 > b_0$ .

For numerical tests, we set the initial ellipse with major axis  $a = 0.4$  and minor axis  $b = 0.3$  on the computational domain  $\Omega = (-1, 1) \times (-1, 1)$ . The other parameters are used as  $\epsilon = \epsilon_8$  and  $\Delta t = 0.001$ . In Fig. 9, we obtain the numerical results of bulk and surface-limited growth models with three different values of  $\lambda_p$ . Here, first and second rows in Fig. 9 represent the contour lines at the level  $\phi(x, y) = 0.5$  and cross-section profiles at  $y = 0$ , respectively.

As shown in Fig. 9, we can see that the surface-limited growth model is more stable than the bulk growth model with regard to larger proliferation rates  $\lambda_p$ . In addition, the numerical results by the our proposed method are comparable to the theoretical results although the proliferation rate is large.

### 4.3. Three-dimensional growth

In the case that the tumor retains its spherical symmetry, we can calculate the problem on a one-dimensional space as shown in Fig. 10.

Similar to that in the radially symmetric case, we obtain the following analytic solution in the spherically symmetric case.

$$r(t) = r(0)e^{\lambda_p t/3}. \tag{26}$$

#### 4.3.1. Temporal evolution of initial sphere

In this section, we investigate the three-dimensional tissue growth. For this, we perform the spherically symmetric and fully three-dimensional simulations.

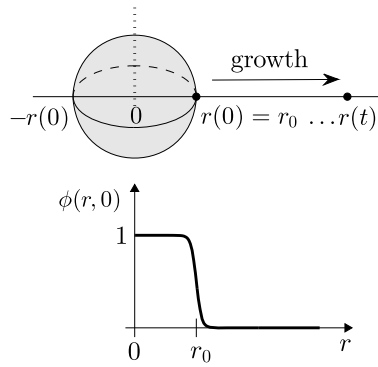


**Fig. 10.** Top: a spherically symmetric three-dimensional tumor with the initial boundary position  $r(0) = r_0$ . Bottom: a computational domain with a spherically symmetric boundary condition at  $r = 0$ .

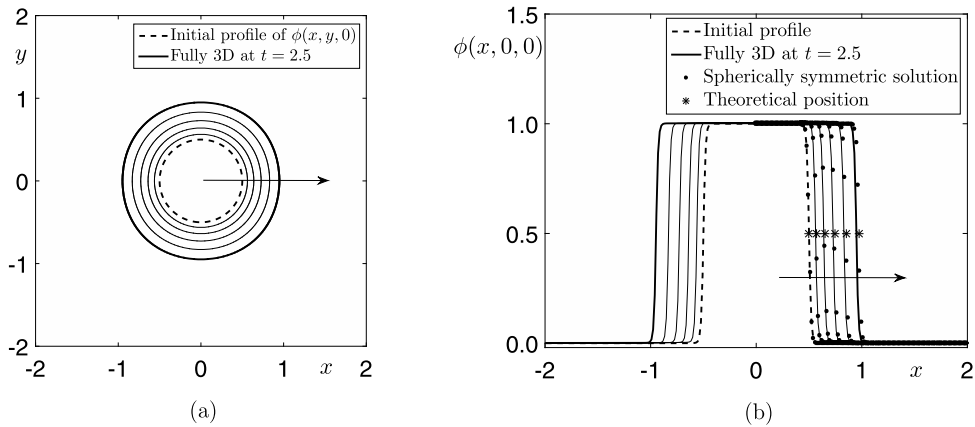


**Fig. 11.** Comparison of spherically symmetric and fully three-dimensional temporal results. (a) Contour lines at the level  $\phi(x, y, 0) = 0.5$  and (b) cross-section profiles of  $\phi(x, 0, 0)$  at  $t = 0, 0.5, 1, 1.5, 2,$  and  $2.5$ . Here, the arrow indicates the increasing time.

The initial conditions are set as

$$\phi(r, 0) = \frac{1}{2} - \frac{1}{2} \tanh\left(\frac{r - 0.5}{2\sqrt{2}\epsilon}\right)$$

for spherically symmetric problem and

$$\phi(x, y, z, 0) = \frac{1}{2} - \frac{1}{2} \tanh\left(\frac{\sqrt{x^2 + y^2 + z^2} - 0.5}{2\sqrt{2}\epsilon}\right)$$

for fully three-dimensional problem. We use a proliferation rate  $\lambda_p = 0.8$ , spatial and temporal step sizes  $h = 1/64$ ,  $\Delta t = 0.0025$ , and a transition layer  $\epsilon = \epsilon_4$ . And the computational domains  $\Omega = (-1, 1)$  and  $\Omega = (-2, 2)^3$  are used for the spherically symmetrical and full three-dimensional tests, respectively.

Fig. 11 shows the temporal solutions for fully three-dimensional and spherically symmetric problems at time  $t = 0, 1, 1.5, 2,$  and  $2.5$ . As we expected, we can observe that the both numerical solutions are propagated by the effect of the proliferation rate.

In Fig. 11(b), we can see that the numerical results for the spherically symmetrical and full three-dimensional tests are in good agreement with the theoretical results, obtained by Eq. (26).

#### 4.3.2. Temporal evolution of initial ellipsoidal tissue

Next, we consider the evolution of an ellipsoidal tumor in the three-dimensional space. The initial ellipsoidal tumor shape is given by

$$\frac{x^2}{a^2} + \frac{y^2}{b^2} + \frac{z^2}{c^2} = 1. \tag{27}$$

By Darcy's law, we assume that the cell velocity  $\mathbf{u} = -\nabla p$ , where  $p$  is the pressure field. By using Eq. (2), we have that

$$-\Delta p = \nabla \cdot \mathbf{u} = \lambda_p. \tag{28}$$

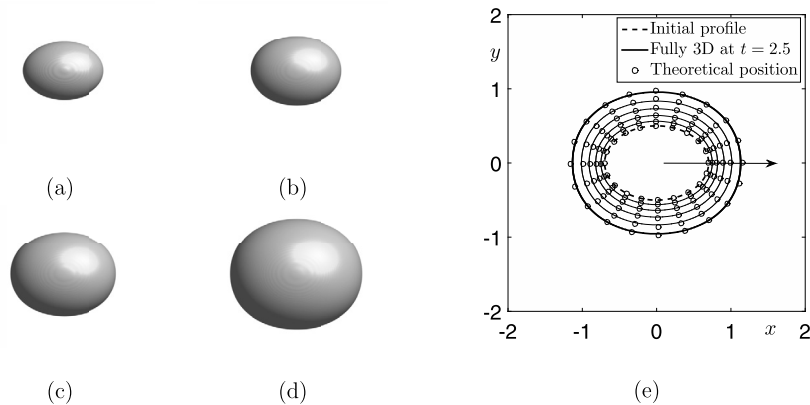


**Fig. 12.** Temporal evolutions of the ellipsoid tissue. (a)–(d): Numerical (isosurface) and theoretical (circled marker) results at times  $t = 0, 0.75, 1.5,$  and  $2.5,$  respectively. (e): Overlapped contour lines of numerical and theoretical results at the level  $\phi(x, y, 0) = 0.5.$

As the pressure field is unique up to constant, we set a zero Dirichlet boundary condition on the moving domain boundary  $\partial\Omega_t,$  where  $\partial\Omega_0 = \{(x, y, z) | x^2/a^2 + y^2/b^2 + z^2/c^2 = 1\}.$  The solution for Eq. (28) is given by

$$p(x, y, z) = -\frac{\lambda_p a^2 b^2 c^2}{2(a^2 b^2 + b^2 c^2 + c^2 a^2)} \left( \frac{x^2}{a^2} + \frac{y^2}{b^2} + \frac{z^2}{c^2} - 1 \right).$$

Furthermore, we have the velocity

$$\mathbf{u}(x, y, z) = -\nabla p(x, y, z) = \frac{\lambda_p}{a^2 b^2 + b^2 c^2 + c^2 a^2} (b^2 c^2 x, c^2 a^2 y, a^2 b^2 z).$$

Let us suppose that  $b = c.$  Then we obtain the following formulae using **Mathematica** software [30],

$$\begin{aligned} a(t) &= \sqrt{1 + (1 + 8e^{2t} + 4\sqrt{e^{2t} + 4e^{4t}})^{-\frac{1}{3}} + (1 + 8e^{2t} + 4\sqrt{e^{2t} + 4e^{4t}})^{\frac{1}{3}}}, \\ b(t) &= [ \{-2 - 8\sqrt{e^{2t} + 4e^{4t}} + (1 + 8e^{2t} + 4\sqrt{e^{2t} + 4e^{4t}})^{\frac{1}{3}} \\ &\quad + 4\sqrt{e^{2t} + 4e^{4t}}(1 + 8e^{2t} + 4\sqrt{e^{2t} + 4e^{4t}})^{\frac{1}{3}} + (1 + 8e^{2t} + 4\sqrt{e^{2t} + 4e^{4t}})^{\frac{2}{3}} \\ &\quad + 8e^{2t}(-2 + (1 + 8e^{2t} + 4\sqrt{e^{2t} + 4e^{4t}})^{\frac{1}{3}})(1 + 8e^{2t} + 4\sqrt{e^{2t} + 4e^{4t}})^{-1} \}^{\frac{1}{2}}, \end{aligned}$$

where we assumed that  $a_0 = 2$  and  $b_0 = c_0 = 1.$

Fig. 12 shows the temporal evolution of the ellipsoidal shape in the fully three-dimensional simulations. The initial condition is given by Eq. (27) with  $a = 0.7, b = 0.5,$  and  $c = 0.4.$  And we use  $256^3$  mesh grid on a  $(-2, 2)^3$  domain with  $\epsilon_4, \lambda_p = 0.8,$  and  $\Delta t = 0.0025.$  In Fig. 12(a)–(d), each isosurface represents a numerical solution for  $t = 0, 0.75, 1.5,$  and  $2.5.$  And the dot means the theoretical value at each times. Furthermore, we overlap its corresponding contour lines at the level  $\phi(x, y, 0) = 0.5$  in Fig. 12(e). Again, we can see that the numerical and theoretical results are in good agreements.

#### 4.4. Application on complex tumor model

In this section, we consider the four-species model representing the tumor cell concentration and the healthy cell concentration along with two species identified with extracellular water, that is, nutrient-rich and nutrient-poor waters [12]. We assume that the mixture is composed of the following four species  $\phi, \psi, n,$  and  $w,$  which are tumor and healthy cell volume fractions, nutrient-rich, and nutrient-poor extracellular water volume fractions, respectively. The mixture is assumed to be saturated as  $\phi + \psi + n + w = 1$  everywhere. With the additional constraint, that is,  $\phi + \psi$  and  $n + w$  are constants everywhere, the total energy can be written as follows.

$$\mathcal{E} = \int_{\Omega} \left( 4\Gamma F'(\phi) + \frac{\epsilon^2}{2} |\nabla \phi|^2 + \chi(\phi, n) + \frac{1}{2\delta} n^2 \right) \mathbf{d}\mathbf{x},$$

where  $\Gamma$  is a positive coefficient for a double well polynomial free energy,  $\chi(\phi, n) = -\chi_0 \phi n$  is the chemotaxis energy and  $\delta$  is a small positive parameter for the relative strength of the interaction between the cell and nutrient species [12]. Now, we obtain the following four-species model.

$$\frac{\partial \phi}{\partial t} = \nabla(M_\phi \nabla \mu) + \gamma_\phi, \tag{29}$$

$$\mu = 4\Gamma F'(\phi) - \epsilon^2 \Delta \phi - \chi_0 n, \tag{30}$$

$$\frac{\partial n}{\partial t} = \nabla(M_n \nabla(-\chi_0 \phi + n/\delta)) + \gamma_n, \tag{31}$$

where  $M_\phi$  and  $M_n$  are mobility functions for  $\phi$  and  $n$ , respectively. Also,  $\gamma_\phi$  is defined as  $\gamma_\phi = P_0 \phi n + \delta P_0 \phi(-\chi_0 \phi - \mu_\phi)$  and  $\gamma_n$  is proposed as  $\gamma_n = -\gamma_\phi$ .

Now, we assume that the nutrient concentration will be taken as quasi-steady, that is,  $n_t = 0$  and Dirichlet boundary conditions will be imposed. Additionally, the mobility functions are given as  $M_\phi = \hat{M}\phi^2$  and  $M_n = \delta \hat{D}$ , where  $\hat{M}$  and  $\hat{D}$  are positive constants. Then, we obtain the following system as

$$\frac{\partial \phi}{\partial t} = \nabla \cdot (\hat{M}\phi^2 \nabla \mu) + \gamma_\phi, \tag{32}$$

$$\mu = F'(\phi) - \epsilon^2 \Delta \phi - \chi_0 n, \tag{33}$$

$$0 = \hat{D} \Delta n - \delta \hat{D} \chi_0 \Delta \phi + \gamma_n, \tag{34}$$

for  $(x, y, t) \in \Omega \times (0, T]$  and the boundary conditions are taken by  $\partial \phi / \partial \mathbf{n} = \partial \mu / \partial \mathbf{n} = 0$  and  $n(x, y, t) = 1$  for  $(x, y, t) \in \partial \Omega \times (0, T]$ . Here,  $\mathbf{n}$  is the outward normal vector to the domain boundary  $\partial \Omega$ .

#### 4.4.1. Numerical solution

By our numerical splitting scheme, we obtain the following numerical solution at each step.

**Step 1)** Calculate the increased mass.

$$\phi_{ij}^* = \phi_{ij}^k + \Delta t \alpha (\phi_{ij}^k) F(\phi_{ij}^k),$$

$$\text{where } \alpha(\phi_{ij}^k) = \frac{e^{\gamma_{ij}^k \Delta t} - 1}{\Delta t} \sum_{i=1}^{N_x} \sum_{j=1}^{N_y} \phi_{ij}^k / \sum_{i=1}^{N_x} \sum_{j=1}^{N_y} F(\phi_{ij}^k),$$

$$\gamma_{ij}^k = P_0 n_{ij}^k \phi_{ij}^k + \delta P_0 \phi_{ij}^k [\chi_0 (n_{ij}^k - \phi_{ij}^k) - F'(\phi_{ij}^k) + \epsilon^2 \Delta_h \phi_{ij}^k].$$

**Step 2)** Solve the modified Cahn–Hilliard equation.

$$\frac{\phi_{ij}^{k+1} - \phi_{ij}^*}{\Delta t} = \nabla_h \cdot (\hat{M}(\phi_{ij}^k)^2 \nabla_h \mu_{ij}^{k+1}),$$

$$\mu_{ij}^{k+1} = F'(\phi_{ij}^{k+1}) - \epsilon^2 \Delta_h \phi_{ij}^{k+1} - \chi_0 n_{ij}^k.$$

**Step 3)** Solve quasi-steady nutrient equation.

$$0 = \delta \hat{D} \Delta_h \left( \frac{n_{ij}^{k+1}}{\delta} - \chi_0 \phi_{ij}^{k+1} \right) - \gamma_{ij}^{k+1},$$

$$\gamma_{ij}^{k+1} = P_0 n_{ij}^k \phi_{ij}^{k+1} + \delta P_0 \phi_{ij}^{k+1} [\chi_0 (n_{ij}^k - \phi_{ij}^{k+1}) - F'(\phi_{ij}^{k+1}) + \epsilon^2 \Delta_h \phi_{ij}^{k+1}].$$

The above equation is rewritten by

$$(\Delta_h n_{ij})^{k+1} = \delta \chi_0 \Delta_h \phi_{ij}^{k+1} + \frac{1}{\hat{D}} \gamma_{ij}^{k+1}.$$

Next, we perform a numerical test to show the nonlinear growth case. For numerical simulation, we use the parameters as  $\hat{M} = 100$ ,  $\hat{D} = 1$ ,  $\delta = 0.01$ ,  $\Gamma = 0.045$ ,  $\chi_0 = 0.05$ ,  $P_0 = 0.1$ ,  $\epsilon = 0.01$ ,  $\Delta t = 0.0025$ , and  $N_x = 512$  on the computational domain  $[-12.6, 12.6] \times [-12.6, 12.6]$ . The initial condition is set to

$$\phi(x, y, 0) = \frac{1}{2} - \frac{1}{2} \tanh \left( \frac{\sqrt{\left(\frac{x}{2.1}\right)^2 + \left(\frac{y}{1.9}\right)^2} - 1.0}{2\sqrt{2}\epsilon} \right).$$

Fig. 13 shows how the elliptic tumor propagates as time evolves. Unlike the previous examples, we can see the irregular growth of the tumor cell.

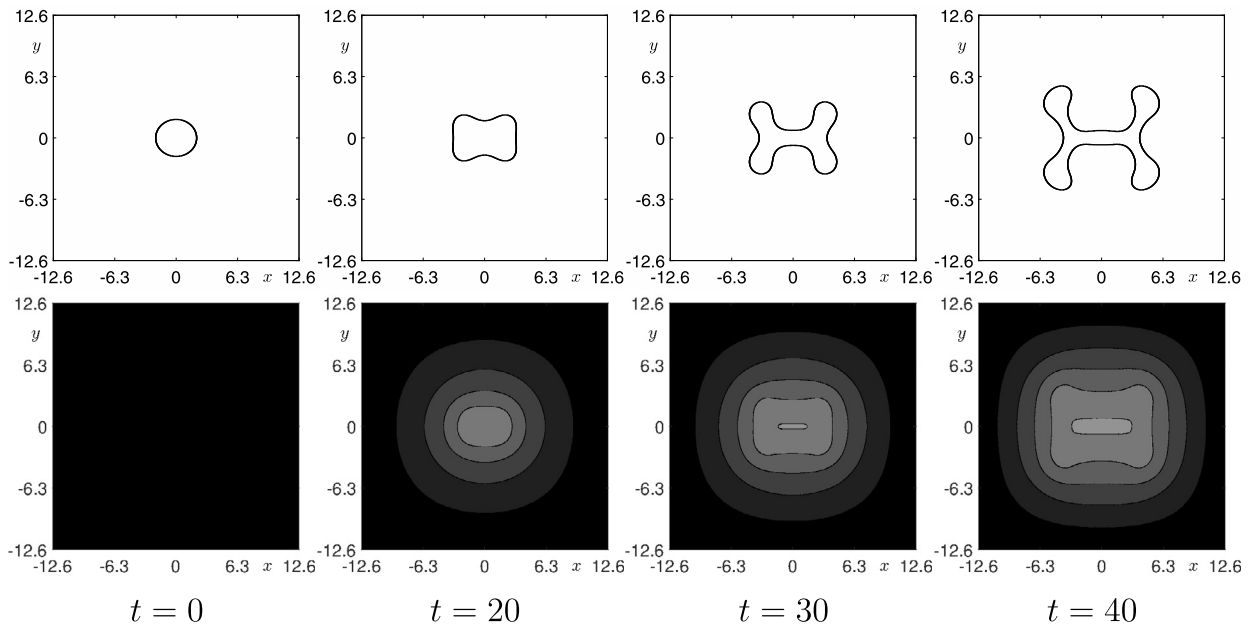


**Fig. 13.** Temporal evolution with nonlinear tissue growth model. Top row: contour line of tumor  $\phi$  at the level  $\phi(x, y) = 0.5$  and bottom row: contour image of nutrient  $n$ . Evolution times are given below each figure.

## 5. Conclusion

In this paper, we considered the modeling of tissue growth by phase-field models, along with their associated numerical methods. Our model is based on the Cahn–Hilliard equation, along with a source term. In order to accurately and efficiently solve the equations, we used an operator splitting method. First, we solved the source term analytically and redistributed the increased mass around the tissue boundary position. Subsequently, we solved the Cahn–Hilliard equation using the nonlinearly gradient stable numerical scheme to make the interface transition profile smooth. We then performed various numerical experiments, confirming a good agreement between the numerical results and the analytical solutions. In future work, we plan to apply our proposed numerical scheme to more complex and comprehensive tumor models.

## Acknowledgements

The authors are grateful to the reviewers whose valuable suggestions and comments significantly improved the quality of this paper. The first author (D. Jeong) was supported by Basic Science Research Program through the National Research Foundation of Korea (NRF) funded by the Ministry of Education, Science and Technology (2014R1A6A3A01009812). The corresponding author (J.S. Kim) was supported by the National Research Foundation of Korea (NRF) grant funded by the Korea government (MSIP) (NRF-2014R1A2A2A01003683).

## References

- [1] D. Ambrosi, L. Preziosi, On the closure of mass balance models for tumor growth, *Math. Models Methods Appl. Sci.* 12 (5) (2002) 737–754.
- [2] J.R. Branco, J.A. Ferreira, P. de Oliveira, Mathematical modeling of efficient protocols to control glioma growth, *Math. Biosci.* 255 (2014) 83–90.
- [3] N.F. Britton, *Essential Mathematical Biology*, Springer, London, 2003.
- [4] J.W. Cahn, On spinodal decomposition, *Acta Metall.* 9 (9) (1961) 795–801.
- [5] J.W. Cahn, J.E. Hilliard, Free energy of a nonuniform system. I. Interfacial free energy, *J. Chem. Phys.* 28 (1958) 258–267.
- [6] Y. Chen, J.S. Lowengrub, Tumor growth in complex, evolving microenvironmental geometries: a diffuse domain approach, *J. Theor. Biol.* 361 (21) (2014) 14–30.
- [7] Y. Chen, S.M. Wise, V.B. Shenoy, J.S. Lowengrub, A stable scheme for a nonlinear, multiphase tumor growth model with an elastic membrane, *Int. J. Numer. Methods Biomed. Eng.* 30 (7) (2014) 726–754.
- [8] D.J. Eyre, An unconditionally stable one-step scheme for gradient systems, Unpublished article, <http://www.math.utah.edu/~eyre/research/methods/stable.ps>, 1983.
- [9] D.J. Eyre, Unconditionally gradient stable time marching the Cahn–Hilliard equation, *Mater. Res. Soc. Symp. Proc.* 529 (1998) 39–46.
- [10] F. Frascaoli, P.S. Kim, B.D. Hughes, K.A. Landman, A dynamical model of tumour immunotherapy, *Math. Biosci.* 253 (2014) 50–62.
- [11] A. Hawkins-Daarud, S. Prudhomme, K.G. van der Zee, J.T. Oden, Bayesian calibration, validation, and uncertainty quantification of diffuse interface models of tumor growth, *J. Math. Biol.* 67 (6–7) (2013) 1457–1485.
- [12] A. Hawkins-Daarud, K.G. van der Zee, J.T. Oden, Numerical simulation of a thermodynamically consistent four-species tumor growth model, *Int. J. Numer. Methods Biomed. Eng.* 28 (1) (2012) 3–24.
- [13] G.E. Kapellos, T.S. Alexiou, A.C. Payatakes, A multiscale theoretical model for diffusive mass transfer in cellular biological media, *Math. Biosci.* 210 (1) (2007) 177–237.

- [14] G.E. Kapellos, T.S. Alexiou, A.C. Payatakes, Theoretical modeling of fluid flow in cellular biological media: an overview, *Math. Biosci.* 225 (2) (2010) 83–93.
- [15] D. Kay, R. Welford, A multigrid finite element solver for the Cahn–Hilliard equation, *J. Comput. Phys.* 212 (1) (2006) 288–304.
- [16] J. Kim, A diffuse-interface model for axisymmetric immiscible two-phase flow, *Appl. Math. Comput.* 160 (2) (2005) 589–606.
- [17] J. Kim, Three-dimensional numerical simulations of a phase-field model for anisotropic interfacial energy, *Commun. Korean Math. Soc.* 22 (3) (2007) 453–464.
- [18] J. Kim, K. Kang, J. Lowengrub, Conservative multigrid methods for Cahn–Hilliard fluids, *J. Comput. Phys.* 193 (2) (2004) 511–543.
- [19] D. Lee, J.Y. Huh, D. Jeong, J. Shin, A. Yun, J. Kim, Physical, mathematical, and numerical derivations of the Cahn–Hilliard equation, *Comput. Mater. Sci.* 81 (2014) 216–225.
- [20] C. Lee, D. Jeong, J. Shin, Y. Li, J. Kim, A fourth-order spatial accurate and practically stable compact scheme for the Cahn–Hilliard equation, *Physica A* 409 (1) (2014) 17–28.
- [21] J.S. Lowengrub, H.B. Frieboes, F. Jin, Y.L. Chuang, X. Li, P. Macklin, S.M. Wise, V. Cristini, Nonlinear modelling of cancer: bridging the gap between cells and tumours, *Nonlinearity* 23 (1) (2010) R1–R91.
- [22] J.T. Oden, A. Hawkins, S. Prudhomme, General diffuse-interface theories and an approach to predictive tumor growth modeling, *Math. Models Methods Appl. Sci.* 20 (3) (2010) 477–517.
- [23] C. Padra, N.N. Salva, Locating multiple tumors by moving shape analysis, *Math. Biosci.* 245 (2) (2013) 103–110.
- [24] G. Sciumè, W.G. Gray, M. Ferrari, P. Decuzzi, B.A. Schrefler, On computational modeling in tumor growth, *Arch. Comput. Methods Eng.* 20 (4) (2013) 327–352.
- [25] G. Tierra, F. Guillén-González, Numerical methods for solving the Cahn–Hilliard equation and its applicability to related energy-based models, *Arch. Comput. Methods Eng.* 22 (2015) 269–289.
- [26] R.D. Travasso, E.C. Poire, M. Castro, J.C. Rodríguez-Manzaneque, A. Hernandez-Machado, Tumor angiogenesis and vascular patterning: a mathematical model, *PLoS ONE* 6 (2011) e19989.
- [27] U. Trottenberg, C.W. Oosterlee, A. Schuller, *Multigrid*, Academic Press, London, 2000.
- [28] S.M. Wise, J.S. Lowengrub, V. Cristini, An adaptive multigrid algorithm for simulating solid tumor growth using mixture models, *Math. Comput. Model.* 53 (1–2) (2011) 1–20.
- [29] S.M. Wise, J.S. Lowengrub, H.B. Frieboes, V. Cristini, Three-dimensional multispecies nonlinear tumor growth? I: model and numerical method, *J. Theor. Biol.* 253 (3) (2008) 524–543.
- [30] *Wolfram Mathematica 8.0.4.0 for Microsoft Windows*, Wolfram Research, Inc., Champaign, IL, USA, 2011.